

Accepted Manuscript

Microstructure and mechanical properties of CVD TiN/TiBN multilayer coatings

Christina Kainz, Nina Schalk, Michael Tkadletz, Christian Mitterer, Christoph Czettl



PII: S0257-8972(19)30463-3
DOI: <https://doi.org/10.1016/j.surfcoat.2019.04.086>
Reference: SCT 24581
To appear in: *Surface & Coatings Technology*
Received date: 9 November 2018
Revised date: 26 April 2019
Accepted date: 27 April 2019

Please cite this article as: C. Kainz, N. Schalk, M. Tkadletz, et al., Microstructure and mechanical properties of CVD TiN/TiBN multilayer coatings, *Surface & Coatings Technology*, <https://doi.org/10.1016/j.surfcoat.2019.04.086>

This is a PDF file of an unedited manuscript that has been accepted for publication. As a service to our customers we are providing this early version of the manuscript. The manuscript will undergo copyediting, typesetting, and review of the resulting proof before it is published in its final form. Please note that during the production process errors may be discovered which could affect the content, and all legal disclaimers that apply to the journal pertain.

Microstructure and mechanical properties of CVD TiN/TiBN multilayer coatings

Christina Kainz¹, Nina Schalk¹, Michael Tkadletz², Christian Mitterer², Christoph Czettel³

¹ *Christian Doppler Laboratory for Advanced Coated Cutting Tools at the Department of Materials Science, Montanuniversität Leoben, Franz-Josef-Straße 18, 8700 Leoben, Austria*

² *Department of Materials Science, Montanuniversität Leoben, Franz-Josef-Straße 18, 8700 Leoben, Austria*

³ *Ceratizit Austria GmbH, Metallwerk-Plansee-Straße 71, 6600 Reutte, Austria*

Keywords: Multilayer, TiBN, CVD, TEM, Micromechanical testing

Abstract

Application of a multilayered coating architecture based on two alternating hard materials provides a strategy to enhance the mechanical properties of hard coatings for the metal cutting industry. Within this work, the mechanical behavior of CVD TiN/TiBN multilayer coatings was correlated with their microstructure and compared to the respective single-layers. Multilayers with different bilayer periods (1400, 800, 300 and 200 nm) were prepared in an industrial-scale thermal CVD plant by alternate variation of the feed gas composition. Complementary X-ray diffraction, Raman spectroscopy and transmission electron microscopy investigations confirmed a dominating face-centered cubic TiN structure, accompanied by hexagonal TiB₂ and amorphous TiB in the B containing coatings. The addition of B and a decreasing bilayer period resulted in a decreasing grain size and increasing hardness. Micromechanical bending tests revealed an increase of strength and fracture toughness with addition of B and increasing layer number. While the highest strength was observed in a TiBN single-layered coating, the multilayered TiN/TiBN with a bilayer period of 200 nm was the hardest and at the same time toughest of the investigated coatings.

1. Introduction

The demand for high cutting speed and feed rates and simultaneous cost efficiency in the metal cutting industry requires, besides substrate materials with high hot hardness, sophisticated coating materials [1,2]. Hard, wear-resistant TiN coatings have been used for more than 40 years to improve the cutting performance and lifetime of cemented carbide cutting inserts [3]. In addition to solid solution strengthening, further hardening of TiN coatings can be realized by grain refinement through addition of dopants such as B [2]. TiBN coatings are commonly applied for cutting of Ti alloys due to their high hardness at elevated temperatures combined with good oxidation and wear resistance [2,4]. Therefore, extensive research has been performed with special regard to the nanocomposite nature of TiBN, which can be prepared by both, physical or chemical vapor deposition (CVD) [5–8].

In addition to multiphase or nanocomposite coatings, multilayers provide a possibility to attain properties difficult to achieve with a conventional single-layer approach [9]. Hardening in multilayers results from prevention of dislocation movement due to interfaces. Toughening is mainly achieved by crack deflection at the interfaces of adjacent layers [10]. Hard yet tough coatings are reported to offer superior wear resistance in real-life applications compared to brittle hard coatings. They may be realized by a multilayer combination of two different hard materials [11]. Though the proficient properties of TiN and TiBN qualify them as suitable candidates for high performance multilayers in cutting applications, few reports have been published so far on CVD TiN/TiBN multilayers [12–15]. Further, no literature can be found where the relationship between the microstructure and the fracture behavior on the microscopic scale with respect to the bilayer period λ is discussed for the given coating system.

Thus, the aim of the present work is to illuminate the effects of B addition and λ in CVD multilayer coatings with alternating TiN and TiBN layers on the chemical and crystallographic

structure as well as on the micromechanical properties. The combinatorial application of sophisticated characterization techniques like transmission electron microscopy and bending tests performed on free-standing coating micro-cantilevers enabled both a detailed insight into the microstructure of the investigated coatings and the identification of the coating with the most favorable mechanical properties for cutting applications.

2. Experimental methods

Coating depositions were carried out in an industrial-scale thermal CVD plant. A gas mixture of TiCl_4 , H_2 , N_2 , BCl_3 and Ar was used to synthesize TiN and TiBN single-layer and TiN/TiBN multilayer coatings. 6, 12, 24 and 40-layered coatings of alternating TiN and TiBN were prepared by interruption of the BCl_3 feed gas flow, whereas the uppermost layer was TiN. Within the B containing layers, the BCl_3 content in the feed gas was adjusted to 0.15 vol.%. In order to prevent B diffusion into the substrate, the coatings were deposited on a $\sim 0.5 \mu\text{m}$ thick TiN base-layer. The process temperature and pressure were held constant throughout the deposition at $900 \text{ }^\circ\text{C}$ and 930 mbar, respectively. The total thickness of the investigated coatings was between 4 and $5 \mu\text{m}$. Therefore, bilayer periods of ~ 1400 , 800, 300 and 200 nm for the 6, 12, 24 and 40-layered coatings, respectively, were obtained. The multilayer coatings are named accordingly to the respective bilayer period. As substrate material, cemented carbide cutting inserts in SEKN 1203 AF-G3 geometry (according to ISO 1832) with 87 wt.% WC, 9 wt.% Co and 4 wt.% mixed carbides were used.

The elemental composition of the coatings was determined by glow discharge optical emission spectroscopy (GDOES) using a Jobin-Yvon Horiba JY10000 spectroscope. Isostatic hot pressed reference materials of different compositions were used for calibration. Surface and cross-section morphology of the single- and multilayer coatings was evaluated using a field

emission gun scanning electron microscope (SEM) of type Zeiss Auriga. Crystallographic analyses were conducted by X-ray diffraction (XRD) with a Bruker AXS D8 Advance diffractometer in grazing incidence geometry (incidence angle 2°). Residual stresses were determined using the $\sin^2 \psi$ method in Ω mode on the (422) reflection with Cu-K α radiation [16]. In the used set-up, the Bragg angle 2θ was kept constant between 124.5° and 127° . The inclination angle of the sample surface normal in regard to the diffraction vector (ψ) was varied in 14 steps from 0 to 58.5° . ψ angles were chosen in that way that the resulting $\sin^2 \psi$ values featured equidistant steps of roughly 0.05 . Elastic constants taken from ref. [17] were subsequently used to obtain the stress from the measured strain [18]. Texture analysis was carried out in Bragg-Brentano geometry and preferred orientation was evaluated by texture coefficients (TC) from the intensities $I(hkl)$ of the measured peaks according to [19]. Texture-free intensities $I_0(hkl)$ of face-centered cubic (fcc) TiN were taken from the ICDD file # 00-038-1420. A total of $n = 7$ peaks were included in the analysis, i.e. (111), (200), (220), (311), (331), (420) and (422). To gain deeper insight into the microstructure of the multilayers, lamellae for transmission electron microscopy (TEM) were prepared by focused ion beam (FIB) milling using an Orsay Physics Cobra Z-05 device. The lamellae were investigated with an FEI Tecnai F20 microscope equipped with a Schottky field emitter (200 kV). For the N K jump ratio micrographs, the pre-edge micrographs were recorded at 385 eV and the post-edge images at 411 eV. Electron energy loss spectroscopy (EELS) was executed in imaging mode. The C2 aperture, objective aperture and entrance aperture for the high resolution Gatan imaging filter were set to $150 \mu\text{m}$, $70 \mu\text{m}$ and 3mm , respectively. Selected area electron diffraction (SAED) was done using an FEI Tecnai 12 microscope operating with an LaB $_6$ cathode (120 kV). The camera length was set to 1000mm and the diffraction aperture to $6 \mu\text{m}$. Complementary information on the phase composition was gained by cross-sectional μ -Raman spectroscopy

using a LabRAM HR800 spectrometer from Horiba Jobin-Yvon. The device was equipped with a frequency-doubled Nd-YAG laser ($\lambda=514.5$ nm). The measurement was performed applying a step size of 250 nm and a spot size of 750 nm.

Coating hardness and Young's modulus were determined by nanoindentation using an Ultra Micro Indentation System (UMIS) from Fischer-Cripps Laboratories operating with a diamond Berkovich tip. Prior to indentation, the surface of the coatings was polished to obtain a smooth surface for a reasonable measurement. To keep the penetration depths $<10\%$ of the film thickness and therefore exclude substrate effects, a plateau test from 10 to 30 mN with a step size of 1 mN was carried out. Data evaluation was conducted accordingly to the method of Oliver and Pharr [20]. In order to gain insight into the fracture behavior of the coatings, micromechanical tests were executed. Two sets of freestanding bending beams, i.e. notched and unnotched, were prepared by FIB machining on an FEI DualBeam Versa 3D device. The dimensions were adjusted to a bending length of ~ 9 μm and a cross-section of $\sim 3 \times 3$ μm^2 . Unnotched beams served for the determination of the fracture stress. Fracture toughness was evaluated on samples with a sharp notch, located in a distance of ~ 1 μm from the cantilever beam support. The planned indentation position was marked by a reticule with the FIB. The bending beams were imaged by scanning probe microscopy using a Hysitron TriboIndenter TI950 and a spheroconical tip. Loading of the bending beams was done at a rate of 1600 $\mu\text{N/s}$. Taking into account the cantilever geometry and measured load-displacement curve, data analysis was performed accordingly to the method of Matoy *et al.* [21]. In order to gain statistical reliable data, a minimum of each three notched and unnotched beams were tested for every coating system. Depth of the notch and fracture cross-sections were evaluated by post-mortem analysis using SEM.

3. Results and discussion

3.1. Microstructure and chemical composition

The elemental analysis of the single-layer coatings showed a stoichiometric composition for fcc-TiN and a mean composition of 5 at.% B, 48 at.% Ti and 47 at.% N for TiBN. Therefore, the composition of the investigated TiBN coating lies within the section TiN-TiB₂-BN in the ternary phase diagram [22], close to the tie-line of TiN-TiB₂. Since the deposition parameters for TiN and TiBN in the single- and multilayer coatings were the same, the composition of the respective layers in the multilayer system was assumed to be equal to the respective single-layer coating.

The surface morphology of the TiN single-layer (Fig. 1a) is characterized by star-shaped and pyramidal grains, which is in accordance to the findings of Wagner *et al.* [23]. These star-shaped crystals have been suggested to originate from the formation of twinned nuclei at the given comparatively low deposition temperature. V-shaped columnar grains, typical for competitive growth, of ~0.5 μm in-plane and a few μm in growth direction can be observed in the cross-section of TiN (Fig. 1d). The TiBN single-layer displays a similar, although finer structure compared to TiN, which is accompanied by needles (Fig. 1b). The fine grained cross-section of TiBN in Fig. 1e reveals a pronounced decrease in crystallite size compared to TiN, which is in good agreement with the existing literature [2,5,7,8,15]. Fig. 1c depicts, representative for the TiN/TiBN multilayers, the surface of the coating with $\lambda = 1400$ nm, showing a similar surface morphology as single-layered TiBN but without any needles. The cross-section micrograph, shown in Fig. 1f, reveals that the large columnar TiN grains are interrupted by small crystallites in the TiBN layers, followed by a renewed growth of columnar grains in the subsequent TiN layer.

In Fig. 2a, the X-ray diffractograms of the coatings are summarized. In the following, the multilayer coatings are named TiN/TiBN with the respective layer number. Standard peak positions of fcc-TiN and hexagonal (h) TiB₂ are marked by dashed lines [24,25]. All reflections of the TiN single-layer correspond to the respective ICDD pattern. The additional small peak at $2\theta = 34.6^\circ$, which is observed in the TiBN single-layer and in the multilayers, can be assigned to the (100) reflection of h-TiB₂. No indication for crystalline BN is apparent in any of the investigated coatings. The lattice parameter - determined by Rietveld refinement - of the herein investigated TiBN single-layer does with 4.25 Å not differ noteworthy from the one of fcc-TiN (4.24 Å). Though the given diffractograms speak against the incorporation of B within the fcc-TiN grains, it cannot fully be ruled out. With respect to the phase composition of TiBN coatings with B contents of ~5 at.%, different conclusions can be found in the existing literature. While Holzschuh and Wagner *et al.* described the formation of h-TiB₂ within TiBN coatings already at low B contents [26,27], Peytavy *et al.* reported a substitution of N by B in fcc-TiN to obtain fcc-Ti(B,N) [28]. In another approach, Dreiling *et al.* suggested the formation of amorphous TiB at B contents ≤ 18 at.%, which was reinforced by Raman spectroscopy [29]. Fig. 2b summarizes the influence of B addition and λ on the full width at half maximum (FWHM) of the X-ray diffraction peaks and the residual stresses. The evaluation of the FWHM, conducted on the (220) peak, confirms the microstructural changes with addition of B and variation of λ . While the sharp diffraction peaks of TiN originate from the coarse grained microstructure, peak broadening in TiBN is due to the smaller size of coherently diffracting domains [27,30]. Rietveld refinement indicated a noteworthy reduced crystallite size of the fcc-phase in the TiBN coating compared to that of the binary TiN coating. Although less pronounced compared to the distinct FWHM increase with addition of B, peak broadening can also be observed with decreasing λ in the multilayers (Fig. 2b). This is associated with the rising number of interfaces, at which grain

growth is interrupted, as can be seen from the SEM cross-section of the multilayer coating with $\lambda = 1400$ nm in Fig. 1c. The tensile residual stresses increase from 433 ± 7 MPa in TiN to 890 ± 28 MPa in TiBN; the stresses in the multilayer coatings spread between these values. Initially, a decrease of λ results in an increase of the residual stresses, from 492 ± 32 MPa in the coating with $\lambda = 1400$ nm to 684 ± 16 MPa in the one with $\lambda = 300$ nm. For the coating with $\lambda = 200$ nm, a slightly decreased tensile stress is observed. According to Holleck *et al.*, different mechanisms have to be taken into account in the evaluation of stresses within multilayer coatings [31]. First, the difference in thermal expansion coefficients of TiN ($9.4 \times 10^{-6} \text{ K}^{-1}$) compared to TiB₂ ($\sim 7.4 \times 10^{-6} \text{ K}^{-1}$) provokes thermal stresses at the interfaces. These are further accompanied by the stresses between the TiN base layer and cemented carbide ($\sim 5.8 \times 10^{-6} \text{ K}^{-1}$) [32–35]. In addition, residual stresses at the various interfaces of TiN and TiB₂ have to be taken into account as well. The texture of the herein investigated coatings changes with the addition of B from texture-free for TiN to a preferred (110) orientation (TC = 2.9) for TiBN. No pronounced influence of λ on the texture is observed in the multilayers, as all of them exhibit a preferred (110) orientation (TC = 3.3 ± 0.2).

To further illuminate the microstructure and phase composition of the multilayers, TEM analyses were performed. In Fig. 3 the related bright field (BF) TEM micrographs and the N K jump-ratios of the respective multilayer coatings are shown. The bright layers in the N K jump-ratio micrographs correspond to a higher concentration of N and therefore to TiN. The in-plane grain size decreases with decreasing λ from 140 ± 50 nm in the coating with $\lambda = 1400$ nm to 75 ± 10 nm in the one with $\lambda = 200$ nm. The observed behavior is in good accordance with the decreasing out-of-plane grain size with decreasing λ observed in the evolution of the FWHM in the XRDs. The electron energy loss near edge structure (ELNES) of the Ti L_{2,3} and N K-edge of the coating with $\lambda = 1400$ nm, which is representative for the multilayers, is given in Fig. 4a. The

presented patterns correspond to signals recorded in a TiN and a TiBN layer, respectively. The Ti $L_{2,3}$ and N K-edge can be unambiguously related to TiN [29,36,37]. From the B K-edge, shown in the insert in Fig. 4a, presence of B within the TiN layers can be concluded. Owing to the highly diffusive nature of B, diffusion from TiBN into TiN layers is not surprising. A further aspect that has to be taken into account is the residence of BCl_3 in the CVD recipient. Though the flow of the B precursor was interrupted in the TiN layers, remnants of BCl_3 in the gas compartment can still be incorporated into the coating. In addition, B carryover from TiBN into TiN layers during FIB preparation cannot entirely be excluded. In addition to the lower intensity of B in TiN compared to TiBN, a difference in the peak shape is apparent in Fig. 4a. It is therefore assumed, that the B atoms in TiN and those in TiBN exist in a different chemical nature. While the B in TiN is incorporated as free B, comparison of the B K-edge of the TiBN layers with those reported in literature indicates the presence of TiB in the given coatings [36]. On the other hand, the signal could also result from a superimposition of the patterns from free B, TiB_2 and/or TiB. In good accordance to the XRD results, no indication for BN was found. The SAED patterns of the multilayer coatings showed spotty rings, which are characteristic for a polycrystalline sample with comparatively coarse grains (Fig. 4b and c). The d-spacings can nevertheless be assigned to the reported fcc-TiN phase and are in good agreement with the findings from XRD. The weak diffuse ring in the center of the pattern indicates the presence of an additional non-crystalline phase.

Cross-sectional μ -Raman spectroscopy was used as a complementary method to XRD and TEM for the investigation of the phase composition within the system Ti-B-N. While detection of TiB upon XRD or SAED is not possible due to its amorphous nature, it is reported to result in a distinct signal in the Raman spectrum [29]. Fig. 5 shows the cross-sectional Raman spectra of single-layered TiN and TiBN as well as the respective layers within the multilayer

coating with $\lambda = 1400$ nm. The Raman signals at 220 cm^{-1} , 312 cm^{-1} and 552 cm^{-1} are attributed to the transversal acoustical, longitudinal acoustical and transversal optical mode, respectively, of TiN. The additional peak at 350 cm^{-1} in the TiBN single-layer can be assigned to TiB, as the presence of h-TiB₂ should result in an additional peak at $\sim 660\text{ cm}^{-1}$ [29,38]. Formation of this compound is reported at low partial pressure of BCl₃ with a comparable feed gas composition as described in the present work [29,39]. The Raman spectrum of a TiBN layer within the multilayer coating with $\lambda = 1400$ nm displays a shoulder at 350 cm^{-1} , indicating the presence of small amounts of TiB also in the investigated multilayer coatings. The lower intensity of the characteristic peak for TiB in the TiBN layer within the multilayer coating compared to monolayered TiBN is assumed to result from the step size (250 nm) and spot size (750 nm), which does not allow to fully exclude influences from the neighboring TiN layers. Complementary XRD, ELNES, SAED and Raman spectroscopy have to be taken into consideration in order to clarify the phase composition in TiBN. Crystallographic investigations corroborate the assumption that additional phases (TiB, TiB₂) to fcc-TiN are formed. Nevertheless, residual free B in fcc-TiN cannot entirely be excluded. The signal of TiB in the Raman spectrum accompanied by the diffuse ring observed in the SAED confirm the formation of amorphous TiB, while XRD clearly displays the presence of h-TiB₂. Thus, it is concluded that the herein investigated TiBN coating consists to the most part of fcc-TiN and, to a small extent, of amorphous TiB and h-TiB₂.

3.2. Mechanical properties

Fig. 6a shows exemplary load-displacement curves, here recorded at 20 mN, of the six investigated coatings. The contact depth decreases both with addition of B to TiN and with decreasing bilayer period, indicating a higher resistance to plastic deformation. This trend is reinforced by the obtained values of coating hardness of the given samples shown in Fig. 6b. The

pronounced hardness increase with addition of B is extensively discussed in the existing literature [2,26,27]. The rise in hardness from 18 ± 2 GPa for TiN to 29 ± 1 GPa for TiBN stems from the smaller crystallite size and consequently is a result of the Hall-Petch effect [40,41]. According to Barna *et al.*, highly-mobile dopants like B may segregate at the grain boundaries of the majority phase, where they prevent coalescence through formation of their own phase [42]. The decrement of λ results in a slight increase of hardness from 28 ± 3 GPa in the multilayered coating with the highest λ to 31 ± 2 GPa in the one with the lowest λ . However, the high distribution of the measurement values does not allow for a clear statement on the evolution of the hardness as a function of λ . The prevention of dislocation motion at the increasing number of interfaces should result in strengthening with decreasing λ . Providing that sharp interfaces are present, bilayer periods of a few nm may enable the formation of superlattices, which may offer ultra-hardness [43]. However, a limitation in CVD is given due to the time needed for the gas exchange, which leads to the formation of less well-defined interfaces. Therefore, λ of the here investigated multilayer coatings was chosen within a range, where both the beneficial effects of low layer thickness and limitation arising from the deposition technique were considered. For the coatings with $\lambda = 1400$ nm and $\lambda = 700$ nm, the indentation depth was too low to cross the first interface between TiN and TiBN. Therefore, the high hardness measured within the indented TiN layer is most probably a result from the observed presence of small amounts of B within this layer. The Young's modulus stays in the magnitude reported for fcc-TiN with the addition of B and slightly decreases with reduction of λ . This behavior is associated with the increasing number of grain boundaries at the layer interfaces and the resulting higher porosity as λ decreases. The hardness to modulus ratio (H^3/E^2), which is related to the elastic strain to failure, allows a rough estimation of the fracture toughness [11]. Fig. 6c depicts the assessment of the H^3/E^2 -ratio of the investigated coatings. Both the addition of B and a decrease of λ result in a

pronounced increase of the described ratio. The underlying phenomena, which influence the fracture toughness, are discussed in the following.

In order to gain knowledge on the material properties at microscopic length scales, micromechanical tests with freestanding bending beams were performed. The geometry of an unnotched FIB fabricated specimen, which were used for the investigation of the fracture stress, is depicted in Fig. 7a. The used experimental setup further allows to determine the fracture toughness of the investigated samples, for which a sharp notch was implemented by FIB milling. Both, fracture stress and toughness were evaluated at the sudden end of the load-displacement curve, where failure of the micro-cantilevers occurred. Fig. 7b displays the evolution of the fracture properties of single-layered TiN and TiBN as well as TiN/TiBN multilayers. The fracture stress increases from 3.9 ± 0.5 GPa in single-layered TiN to 7.3 ± 0.1 GPa in TiBN. Daniel *et al.* reported the strength of TiN coatings prepared by magnetron sputtering to be between 1.6 and 2.9 GPa depending on density and grain boundary design [44]. The higher strength value of TiN in the present work can be assigned to the different deposition technique and the dense microstructure resulting from the given deposition parameters. While TiN, TiB and TiB₂ all possess mixed ionic-covalent bonding character, the covalent bond fraction is higher in Ti-B compared to Ti-N. This is reflected by the higher strength of TiBN compared to TiN coatings. The maximum fracture stress in the multilayer coatings slightly increases with decreasing λ from a minimum value of 4.7 ± 0.5 GPa in the coating with $\lambda = 800$ nm to 5.8 ± 0.5 GPa in the one with $\lambda = 200$ nm. Thus, the strength of all multilayers spreads between the values observed in single-layered TiN and TiBN. Despite the small increment of fracture stress with increasing layer number, the strength is obviously much more affected by the chemical composition compared to the layered architecture. The fracture strain of the single- and multilayer coatings, which corresponds to the ultimate strain of the cantilever before fracture, is

roughly ~ 1 % for all of them. This low value is explained by the high Young's modulus and the brittle material properties of the herein investigated coatings.

Fracture toughness is of major importance in order to meet the high demands for hard coatings in metal cutting applications. In accordance with the improved hardness and strength with addition of B, the fracture toughness obtained from load-displacement curves for notched bending beams increases from $2.2 \pm 0.4 \text{ MPa m}^{1/2}$ for TiN to $5.0 \pm 0.3 \text{ MPa m}^{1/2}$ for TiBN. The improved fracture toughness of TiBN is associated with the presence of additional B-rich phases and the associated observed grain refinement. The superior fracture toughness in multilayer coatings relies on the deflection of cracks at the various interfaces of adjacent layers and the resulting delayed failure [10]. The increase of fracture toughness with decreasing λ verifies the energy dissipation on the crack tip between the respective layers. For the investigated specimens, the highest fracture toughness was observed in the multilayer with $\lambda = 200 \text{ nm}$ showing a K_{IC} value of $5.8 \pm 0.5 \text{ MPa m}^{1/2}$. The other multilayers display a fracture toughness lower than the one observed in single-layered TiBN. The H^3/E^2 -ratio therefore allowed a good estimation on the effect of B addition and multilayering on the elastic strain to failure. Nevertheless, the H^3/E^2 -estimation indicated a higher fracture toughness compared to single-layered TiBN already in the coating with $\lambda = 800 \text{ nm}$. This mismatch though is not surprising owing to the different measurement principles, i.e. nanoindentation and micromechanical bending tests. Post-mortem analysis of the fracture cross-sections, which are displayed in Fig. 7c, allow a deeper insight into the failure mechanisms. Though all of the herein investigated coatings are ceramics and therefore generally display brittle material behavior, differences in the fracture cross-sections enable to explain the varying K_{IC} values. The fracture morphology of TiN suggests an inter-columnar fracture mechanism along the columnar TiN grain boundaries. This behavior is in accordance with the observations of Bhowmick *et al.* and results from the low cohesive energy between the

individual columnar TiN grains [45,46]. In contrast, in single-layered TiBN crack propagation through the coating is inhibited by the small-grained structure, which is also true for the multilayers with low λ . Within these coatings, the blurred fracture morphology can be associated with an onset of ductile fracture behavior.

4. Conclusions

Single-layered TiN and TiBN as well as four TiN/TiBN multilayers with different bilayer period λ (1400, 800, 300 and 200 nm) were grown by thermal CVD and their microstructure, phase composition and mechanical properties were investigated. The phase composition of TiBN layers within a multilayer stack was examined using a combinatorial approach of X-ray diffraction, ELNES analysis, selected area electron diffraction and Raman spectroscopy and was found to consist of primarily fcc-TiN, co-existing with small amounts of h-TiB₂ and amorphous TiB. While the Young's modulus decreased with decreasing λ , both B addition and increasing layer number resulted in an increase of hardness. Miniature bending tests indicated a stronger dependence of the micromechanical properties on the phase composition compared to the coating architecture. Although less pronounced compared to the distinct increase with addition of B, an increase of the strength was observed with decreasing λ in the multilayers. The fracture toughness showed a strong dependence, both on the elemental composition and the layered coating architecture and was highest in the coating with $\lambda = 200$ nm. Complementary nanoindentation and micromechanical bending tests lead to the conclusion that TiN/TiBN multilayers with small λ might offer high performance gains in cutting applications compared to single-layered TiN and TiBN.

Acknowledgements

The authors want to thank Bernhard Sartory (Materials Center Leoben) for the FIB and Dr. Walter Costin (Materials Center Leoben) for SEM work. Further, Dr. Marco Deluca (Materials Center Leoben) is acknowledged for the cross-sectional μ -Raman measurement, Gerhard Hawranek (Montanuniversität Leoben) for SEM work and Dr. Ilse Letofsky-Papst (Graz University of Technology) for the TEM investigations. The financial support by the Austrian Federal Ministry for Digital and Economic Affairs and the National Foundation for Research, Technology and Development is gratefully acknowledged.

References

- [1] W. Wallgram, U. Schleinkofer, Synthesis, structure, and behaviour of a new CVD TiB₂ coating with extraordinary properties for high performance applications, in: L.S. Sigl, P. Rödhammer, H. Wildner (Eds.), 17th Int. Plansee Seminar, Reutte, Austria, p. HM32.
- [2] H. Holzschuh, Thin Solid Films 469-470 (2004) 92–98.
- [3] W. Schintlmeister, W. Wallgram, J. Kanz, K. Gigl, Wear 100 (1984) 153–169.
- [4] P.H. Mayrhofer, M. Stoiber, C. Mitterer, Scripta Mater. 53 (2005) 241–245.
- [5] C. Mitterer, P.H. Mayrhofer, M. Beschliesser, P. Losbichler, P. Warbichler, F. Hofer, P.N. Gibson, W. Gissler, H. Hruby, J. Musil, J. Vlček, Surf. Coat. Technol. 120-121 (1999) 405–411.
- [6] P.H. Mayrhofer, C. Mitterer, Surf. Coat. Technol. 133-134 (2000) 131–137.
- [7] P. Losbichler, C. Mitterer, P.N. Gibson, W. Gissler, F. Hofer, P. Warbichler, Surf. Coat. Technol. 94-95 (1997) 297–302.

- [8] H. Holzschuh, Moderate Temperature CVD Coatings in the Ti-B-N system, in: G. Kneringer, P. Rödhammer, H. Wildner (Eds.), in: 16th International Plansee Seminar, Plansee Holding AG, Reutte, 2005, p. HM59.
- [9] L. Hultman, J.-E. Sundgren, Structure/Property Relationships for Hard Coatings, in: R.F. Bunshah (Ed.), Handbook of Hard Coatings, Noyes Publications, Park Ridge, New Jersey, 2001.
- [10] Y.X. Wang, S. Zhang, Surf. Coat. Technol. 258 (2014) 1–16.
- [11] A. Leyland, A. Matthews, Wear 246 (2000) 1–11.
- [12] M. Stoiber, E. Badisch, C. Lugmair, C. Mitterer, Surf. Coat. Technol. 163–164 (2003) 451–456.
- [13] M. Stoiber, C. Mitterer, T. Schoeberl, E. Badisch, G. Fontalvo, J. Vac. Sci. Technol. B 21 (2003) 1084–1091.
- [14] M. Stoiber, S. Perlot, C. Mitterer, M. Beschliesser, C. Lugmair, R. Kullmer, Surf. Coat. Technol. 177–178 (2004) 348–354.
- [15] M. Tkadletz, N. Schalk, C. Mitterer, J. Keckes, M. Pohler, C. Czettl, Int. J. Refract. Met. Hard Mater. 71 (2018) 280–284.
- [16] U. Welzel, J. Ligot, P. Lamparter, A.C. Vermeulen, E.J. Mittemeijer, J. Appl. Crystallogr. 38 (2005) 1–29.
- [17] J. Almer, U. Lienert, R.L. Peng, C. Schlauer, M. Odén, J. Appl. Phys. 94 (2003) 697–702.
- [18] I.C. Noyan, J.B. Cohen, Residual Stress: Measurement by Diffraction and Interpretation, Springer-Verlag, New York, 1987.
- [19] M.H. Müller, W.P. Chernock, P.A. Beck, Trans. Metall. Soc. AIME. 212 (1958) 39–40.
- [20] W.C. Oliver, G.M. Pharr, J. Mater. Res. 7 (1992) 1564–1583.

- [21] K. Matoy, H. Schönherr, T. Detzel, T. Schöberl, R. Pippan, C. Motz, G. Dehm, *Thin Solid Films* 518 (2009) 247–256.
- [22] H. Nowotny, F. Benesovsky, C. Brukl, O. Schob, *Monatsh. Chem.* 92 403–414.
- [23] J. Wagner, C. Mitterer, M. Penoy, C. Michotte, W. Wallgram, M. Kathrein, *International Journal of Refractory Metals and Hard Materials* 26 (2008) 120–126.
- [24] International Centre for Diffraction Data, PDF-2 Release, Card number 00-038-1420, 2018.
- [25] International Centre for Diffraction Data, PDF-2 Release, Card number 03-065-1073, 2018.
- [26] H. Holzschuh, *Int. J. Refract. Met. Hard Mater.* 20 (2002) 143–149.
- [27] J. Wagner, D. Hochauer, C. Mitterer, M. Penoy, C. Michotte, W. Wallgram, M. Kathrein, *Surf. Coat. Technol.* 201 (2006) 4247–4252.
- [28] J.L. Peytavy, A. Lebugle, G. Montel, *High Temperatures - High Pressures* 10 (1978) 341–345.
- [29] I. Dreiling, C. Raisch, J. Glaser, D. Stiens, T. Chassé, *Surf. Coat. Technol.* 206 (2011) 479–486.
- [30] B.D. Cullity, *Elements of X-ray Diffraction*, Addison-Wesley, Reading Massachusetts, 1978.
- [31] H. Holleck, M. Lahres, P. Woll, *Surf. Coat. Technol.* 41 (1990) 179–190.
- [32] R.G. Munro, *J. Res. Natl. Inst. Stand. Technol.* 105 (2000) 709–720.
- [33] H.O. Pierson, *Handbook of refractory carbides and nitrides: properties, characteristics, processing, and applications*, Noyes Publications, New York, 1996.
- [34] S. Madtha, C. Lee, K.S. Ravi Chandran, *J. Am. Ceram. Soc.* 91 (2008) 1319–1321.
- [35] H. Wang, T. Webb, J.W. Bitler, *Int. J. Refract. Met. Hard Mater.* 49 (2015) 170–177.
- [36] A. Gupper, A. Fernández, C. Fernández-Ramos, F. Hofer, C. Mitterer, P. Warbichler, *Monatsh. Chem.* 133 (2002) 837–848.

- [37] C. López-Cartes, D. Martínez-Martínez, J.C. Sánchez-López, A. Fernández, A. García-Luis, M. Brizuela, J.I. Oñate, *Thin Solid Films* 515 (2007) 3590–3596.
- [38] I. Dreiling, A. Haug, H. Holzschuh, T. Chassé, *Surf. Coat. Technol.* 204 (2009) 1008–1012.
- [39] M. Nadal, T. Grenet, F. Teyssandier, *J. Phys. IV France* 03 (C5) (1993) 809–814.
- [40] E.O. Hall, *Proc. Phys. Soc. Lond.* 64 (1951) 747–753.
- [41] N.J. Petch, *J. Iron Steel Inst. London.* 173 (1953) 25–28.
- [42] P.B. Barna, M. Adamik, J. Lábár, L. Kövér, J. Tóth, A. Dévényi, R. Manaila, *Surf. Coat. Technol.* 125 (2000) 147–150.
- [43] S. Zhang, D. Sun, Y. Fu, H. Du, *Surf. Coat. Technol.* 167 (2003) 113–119.
- [44] R. Daniel, M. Meindlhumer, W. Baumegger, J. Zalesak, B. Sartory, M. Burghammer, C. Mitterer, J. Keckes, *Acta Mater.* 122 (2017) 130–137.
- [45] S. Bhowmick, Z.-H. Xie, M. Hoffman, V. Jayaram, S.K. Biswas, *J. Mater. Res.* 19 (2004) 2616–2624.
- [46] A. Zeilinger, J. Todt, C. Krywka, M. Müller, W. Ecker, B. Sartory, M. Meindlhumer, M. Stefanelli, R. Daniel, C. Mitterer, J. Keckes, *Sci. Rep.* 6 (2016) 22670.

Figure captions

Fig. 1: SEM surface (top) and cross-section morphology (bottom) of (a,d) the TiN and (b,e) the TiBN (5 at.% B) single-layers and (c,f) the TiN/TiBN coating with $\lambda = 1400$ nm representative for the multilayers.

Fig. 2: a) Grazing incidence X-ray diffractograms and (b) FWHM and residual stresses of TiN and TiBN single-layers and TiN/TiBN multilayers.

Fig. 3: BF-TEM micrographs (left) and NK jump-ratios (right) of the TiN/TiBN coatings with $\lambda =$ (a) 1400, (b) 800, (c) 300 and (d) 200 nm.

Fig. 4: TEM investigation of the TiN/TiBN multilayer coating with $\lambda = 1400$ nm: (a) N K, Ti L_{2,3} edge and B K edge. SAED patterns with respective observed crystal planes of the multilayer coatings with (b) $\lambda = 1400$ nm and (c) $\lambda = 200$ nm

Fig. 5: Cross-sectional μ -Raman spectra of TiN and TiBN single-layers and the TiN/TiBN multilayer coating with $\lambda = 1400$ nm.

Fig. 6: (a) Exemplary load-displacement curves of TiN and TiBN single-layers and TiN/TiBN multilayers recorded at a load of 20 mN. (b) Evolution of hardness and Young's modulus as a function of the bilayer period in comparison to the respective single-layers. (c) The H^3/E^2 ratio as a measure of the resistance to plastic deformation for the TiN and TiBN single-layers and the TiN/TiBN multilayers.

Fig. 7: (a) SE micrograph of an unnotched bending beam in top view. (b) Fracture stress and toughness of TiN and TiBN single-layers and the TiN/TiBN multilayers. (c) SE micrographs of post-mortem fracture cross-sections of unnotched bending beams.

Highlights

- Bilayer period λ in CVD TiN/TiBN multilayer coatings was systematically varied
 - Coatings are dominated by crystalline TiN with fractions of TiB₂ and amorphous TiB
 - Amorphous TiB detected in multilayer stack by cross-sectional Raman spectroscopy
 - TiBN single layer yielded the highest fracture stress
- TiN/TiBN multilayer with lowest λ shows highest hardness and fracture toughness

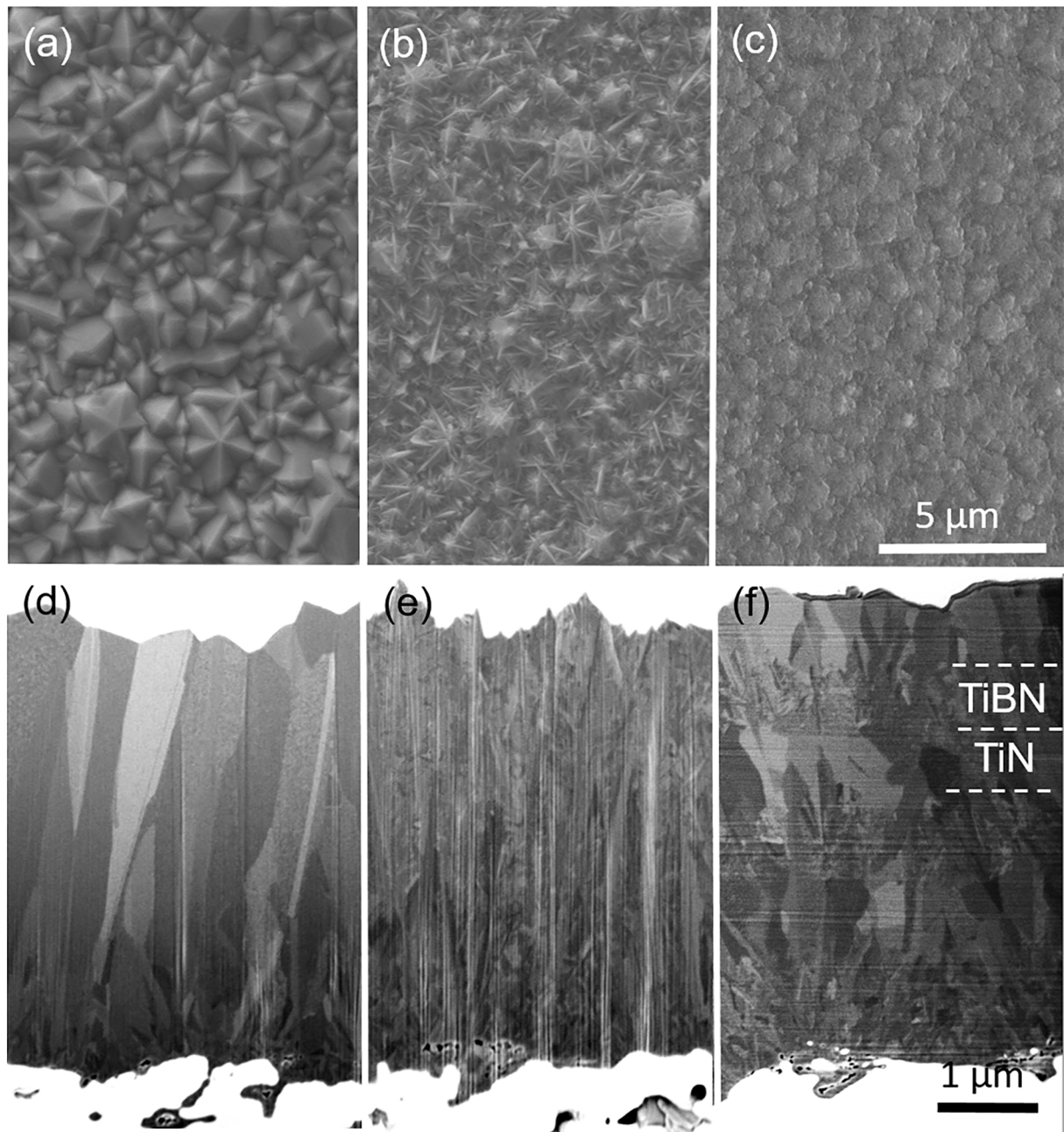


Figure 1

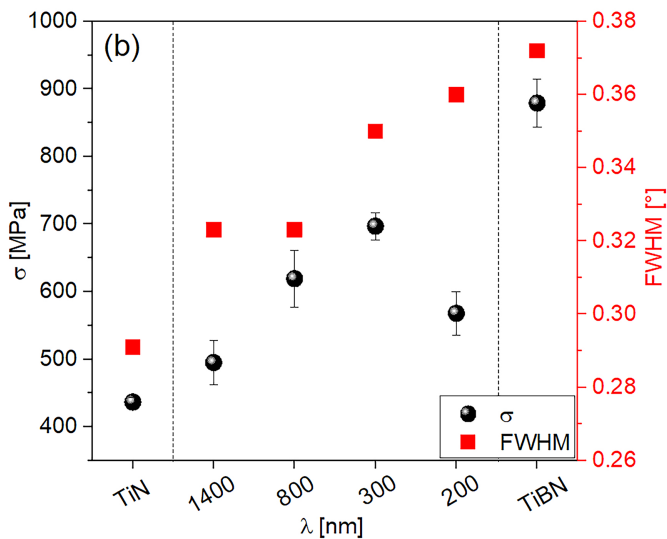
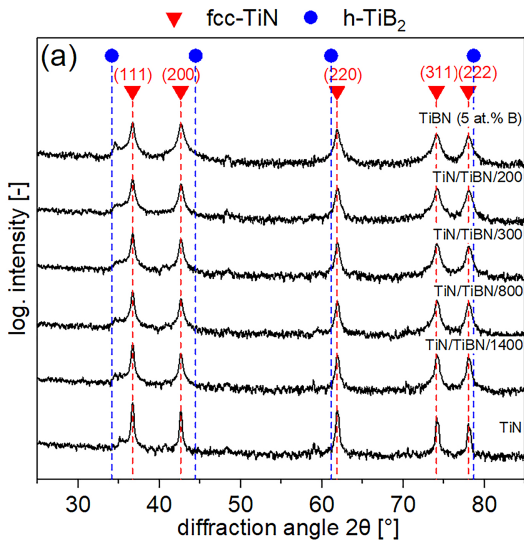


Figure 2

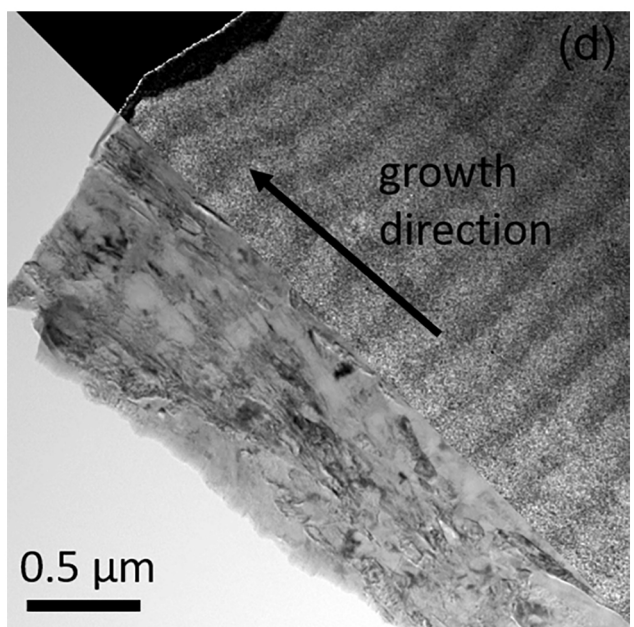
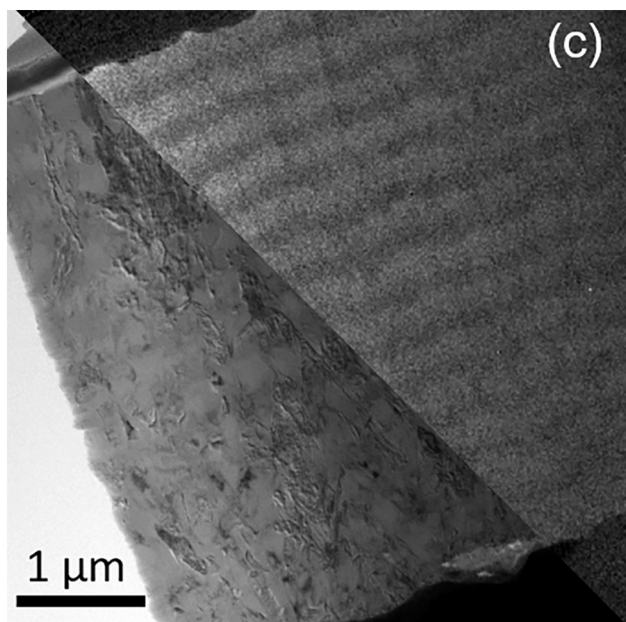
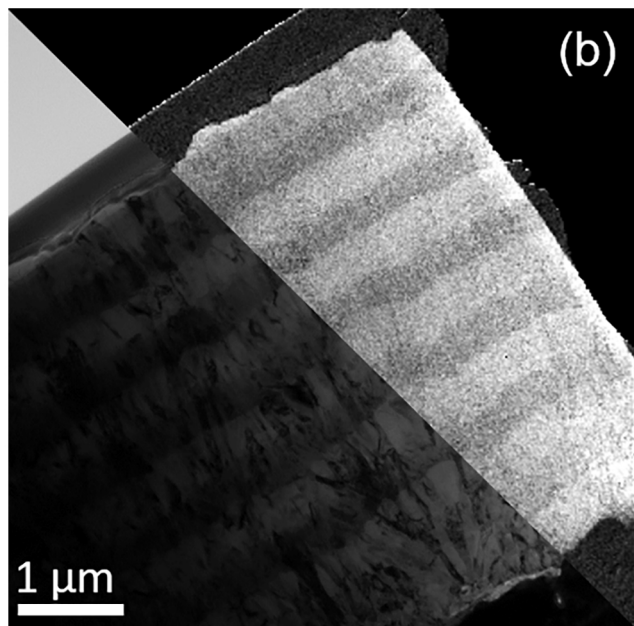
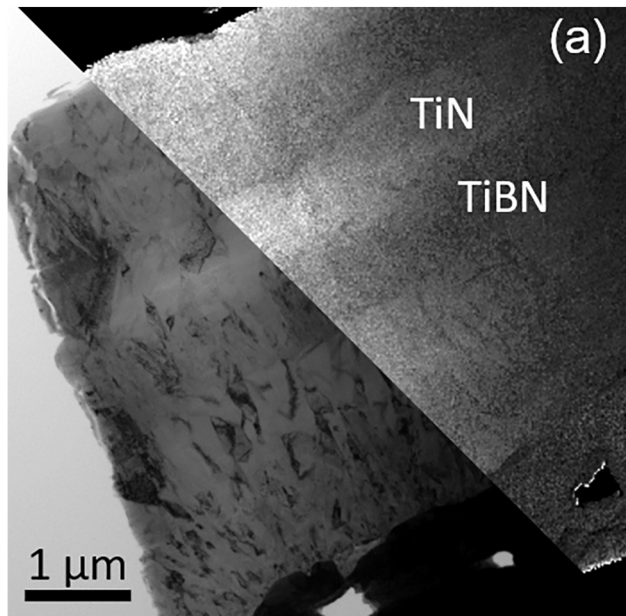


Figure 3

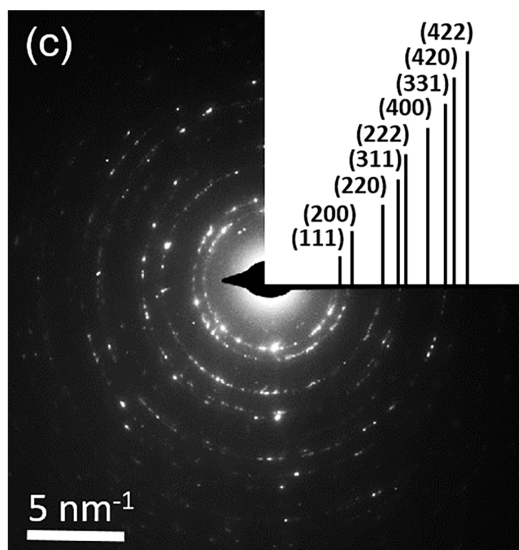
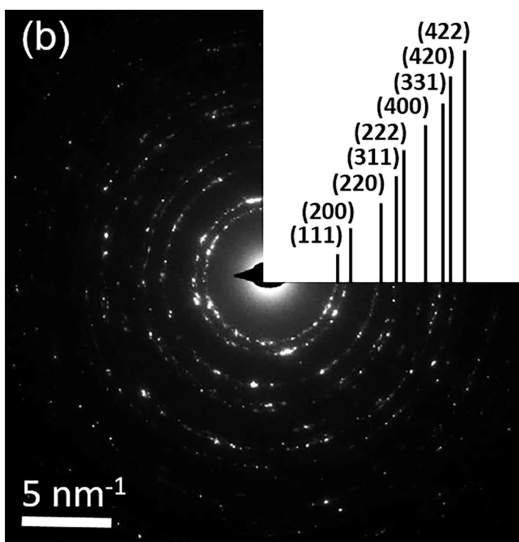
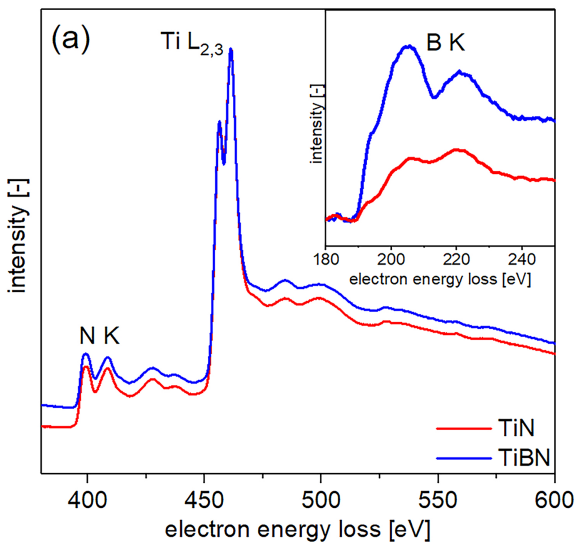


Figure 4

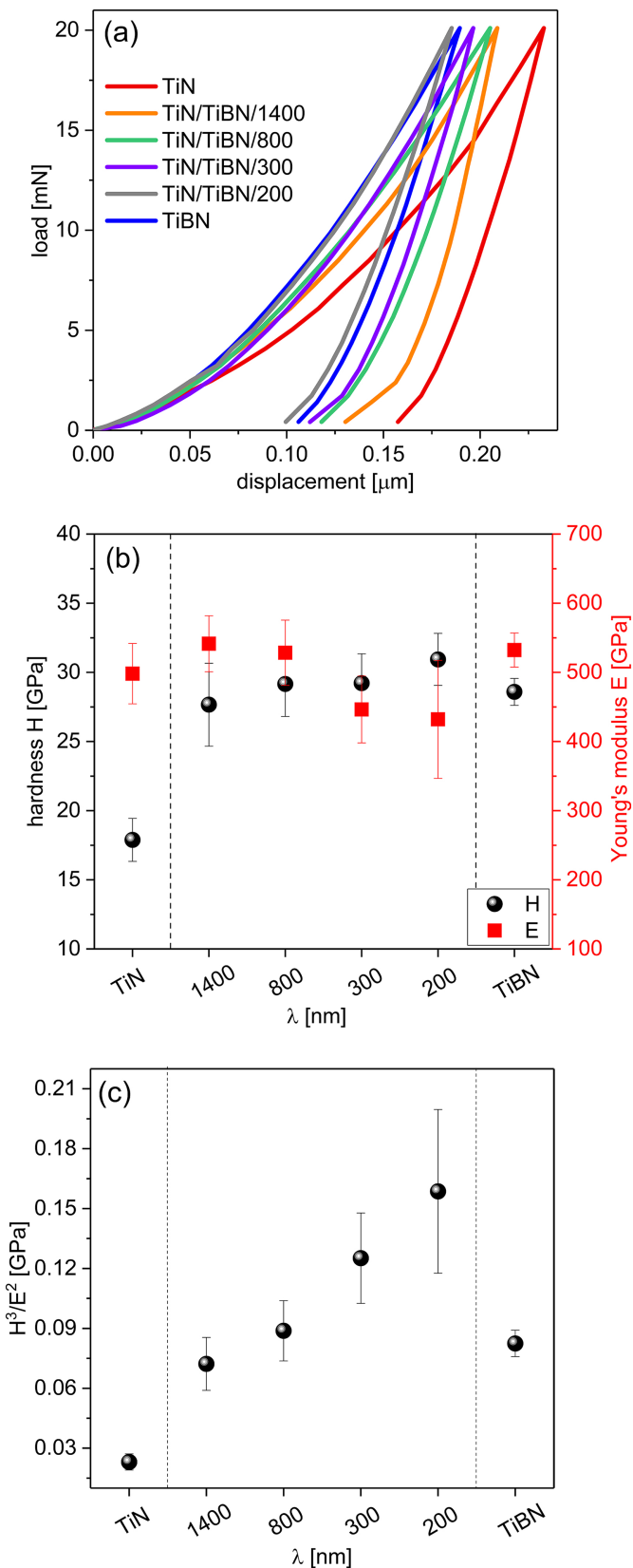
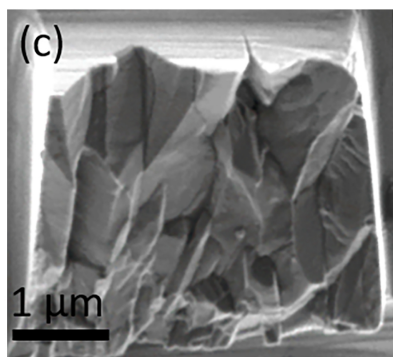
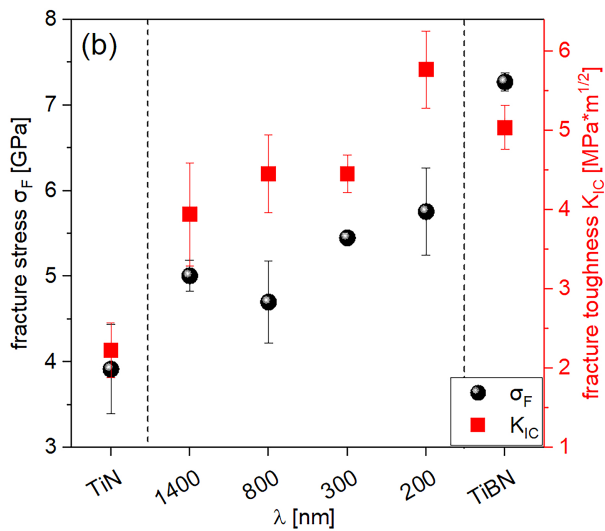
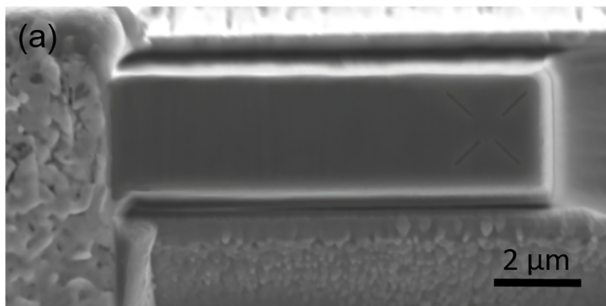
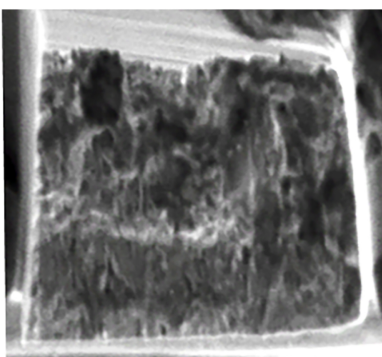


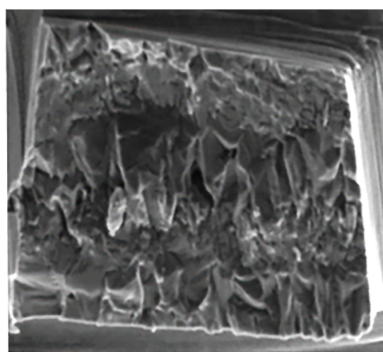
Figure 5



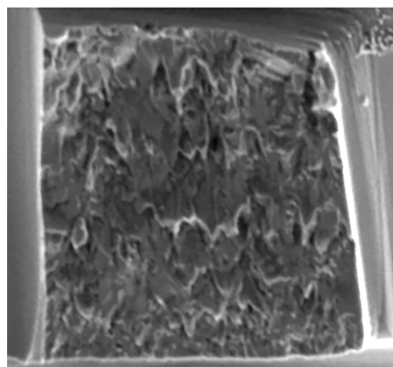
TiN



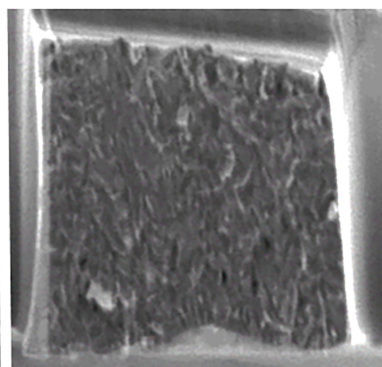
TiBN
5 at.% B



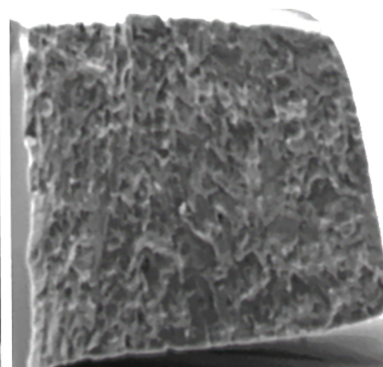
TiN/TiBN/1400



TiN/TiBN/800



TiN/TiBN/300



TiN/TiBN/200

Figure 6